Journal of the Optical Society of America B
OPTICAL PHYSICS

Rational design of colorimetric sensing for a customer-oriented index range using plasmonic substrates

Lin Cheng,[1] Jianyong Mao,[1] Kun Wang,[1] Jiangbo Lu,[2] Kun Huang,[3] Yanpeng Zhang,[1] and Lei Zhang[1,*]

[1]Key Laboratory for Physical Electronics and Devices of the Ministry of Education & Shaanxi Key Lab of Information Photonic Technique, School of Electronic Science and Engineering, Xi'an Jiaotong University, Xi'an 710049, China
[2]School of Physics and Information Technology, Shaanxi Normal University, Xi'an 710062, China
[3]Key Laboratory of Instrumentation Science & Dynamic Measurement, Ministry of Education, School of Instrument and Electronics, North University of China, Taiyuan 030051, China
*Corresponding author: eiezhanglei@xjtu.edu.cn

Received 6 August 2019; revised 19 September 2019; accepted 29 September 2019; posted 2 October 2019 (Doc. ID 374822); published 28 October 2019

Both beneficial matter and harmful matter widely spread in aqueous solutions. Various approaches have been developed to identify them qualitatively and quantitatively. In particular, colorimetric sensing, relying on an observable environment-induced color change, is a readily accessible approach to detect signals via our naked eyes, with no need for extra optoelectronic devices. Here we propose a colorimetric sensing scheme with enhanced performance using plasmonic metasurfaces. By judiciously selecting the structure parameters, the plasmonic resonance can be flexibly tuned at the entire visible range. Along with a pair of polarizers to filter the polarization states of the incident light and output reflection, a plasmonic metasurface, supporting bright colors, can serve as an efficient colorimetric sensing substrate. As an example, a figure of merit can be obtained as high as 1175°/RIU in the demodulation of the hue. Significantly, the sensing capability can be designed according to the selected solvent with a specified refractive index, which promises a target-oriented colorimetric sensing scheme.

https://doi.org/10.1364/JOSAB.36.003168

1. INTRODUCTION

Efficient identification of certain analytes in various solutions is of great importance for both science and engineering communities. Various approaches have been developed to detect either known or unknown targets qualitatively or quantitatively based on different mechanisms. Among them, plasmonic effects give rise to excellent performance at monitoring the analyte with trace concentration in samples, which can be attributed to the strong electromagnetic field localized around the subwavelength structures. Any changes to the immediate dielectric environment could affect the near-field distribution of plasmonic resonances and thus lead to a variation of resonant spectrum in the far field. Therefore, the properties of the plasmonic resonance, such as resonant wavelength, angle, phase, etc., could be employed as a characteristic parameter for sensing purposes [1–9]. In particular, when the resonance occurs in the visible range, the resulting change in spectrum will be transformed to a variation on an observable color, which can thus be employed as an indicator for sensing purposes, usually termed colorimetric sensing [10–13]. Many researches are devoted to designing high-sensitivity systems using various structures such as hyperbolic metamaterials [14], plasmonic nanoholes [15], all-dielectric silicon-based metasurfaces [16], coupled plasmonic cavities [17], and silver quadrumer [18]. In comparison with other types of sensing methods, colorimetric sensing could straightforwardly indicate the existence of the target even quantitatively with no need for extra optoelectronic devices [10,15], although the required resonances are confined to occurring in visible light [10,19,20].

Usually, a specific target analyte will be diluted in an aqueous solution for characterization [14,15,21,22]. In particular, when the amount of analyte is trivial, only a tiny refractive index change will be added to that of the solvent. The resulting color change will thus be difficult to observe. Therefore, it is necessary to design a sensing substrate with an optimized figure of merit (FOM) for a specific aqueous solution with resonance in visible light. Importantly, to obtain bright and vivid colors, a narrow resonance linewidth and low background are preferable [10]. In addition, aluminum (Al) shows advantageous properties as

plasmonic substrates, and it supports resonances covering the entire visible range and longer shelf life when compared with gold and silver [23].

Here we propose a plasmonic Al structure with periodic nanoholes as a colorimetric sensing substrate. A peak-like reflection spectrum can greatly enhance the contrast of color variation using a polarizer-analyzer configuration. Therefore, vibrant colors ranging from blue, to green, to red can be easily observed in a bright light environment due to the negligible reflection background. A FOM, defined as the ratio of index-induced color hue change over the refractive index change [10], reaches as high as 512°/RIU in the entire visible range. Furthermore, a higher FOM of 1175°/RIU is demonstrated within a small index change. It is found that an optimized sensing performance at a specific refractive index range (i.e., solvent) can be achieved by tuning the geometric parameters or excitation conditions.

2. RESULTS AND DISCUSSION

As schematically shown in Fig. 1, two-dimensional (2D) periodic Al rectangular hole arrays are employed as the plasmonic colorimetric sensing substrate, which could support propagating surface plasmon polaritons (SPPs). Due to their strong localization, plasmonic fields at a metal surface could play as an efficient effect to discriminate the optical change of its immediate surrounding [24]. SPPs can be excited only when the momentum matching condition is fulfilled, which is given by [25,26]

$$\left(\frac{2\pi}{\lambda}\sqrt{\frac{\varepsilon_m n_a^2}{\varepsilon_m + n_a^2}}\right)^2 = \left(\frac{2\pi}{\lambda} n_a \sin\theta_i + m\frac{2\pi}{P_x}\right)^2 + \left(n\frac{2\pi}{P_y}\right)^2, \quad (1)$$

where ε_m is the permittivity of Al derived from experiment data [27] and n_a is the refractive index of the immediate environment; (m, n) are integers defining the Bragg diffraction orders; and P_x and P_y are the periodicities along the x and y axes, respectively. All simulations are performed using Lumerical FDTD solutions. Periodic boundary conditions are employed along the x and y axes; perfectly matched layers (PMLs) are applied along the z axis. The structure is excited by a broadband plane wave source ranging from 380 to 780 nm. In order to obtain accuracy results, the mesh size is optimized after a converging test. The polarization state φ_1 of the incident plane wave is fixed at 45°. Therefore, only half of the incident energy is employed to excite the SPP mode, and the electric field is mainly localized around holes [28,29]. Since $|\varepsilon_m| \gg n_a^2$, the resonance wavelength $\lambda_{(-1,0)}$ for $(-1, 0)$ SPP mode can be approximated, expressed as

$$\lambda_{(-1,0)} \approx n_a(1 + \sin\theta_i) P_x. \quad (2)$$

When the environment is vacuum ($n_a = 1$), there is a resonance dip occurring at 419 nm, which arises from the diffraction of $(-1, 0)$ order. To characterize the sensing performance, the immediate environment is then set to be aqueous with a refractive index ranging from 1.33 to 1.47. As the refractive index of the environment increases to 1.33, i.e., a distilled water environment, the reflection dip shifts to 550 nm. Sensitivity S, defined as $\Delta\lambda/\Delta n_a$, of 397 nm/RIU can be obtained. According to Eq. (2), the sensitivity can be expressed as $S = (1 + \sin\theta_i)\ P_x$. When $\vartheta_i = 20°$, the calculated sensitivity is 402 nm/RIU, which matches well with the simulation result. According to Eq. (1), the periodicity P_x is limited at visible range to generate a color, so the corresponding sensitivity is moderate, in comparison with those with a periodicity of ~ 1000 nm. However, to characterize the colorimetric sensing performance, we will focus on the hue variation in color space, and the FOM is defined in demodulation of the hue later.

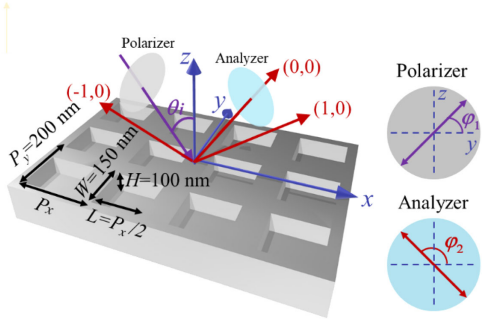

Fig. 1. Schematic of the proposed colorimetric sensing design and polarizer-analyzer configuration for controlling the polarization states of input light and output signal. The physical parameters, i.e., the length L, width W, height H of the nanohole, the periodicities along the x axis P_x and y axis P_y, and the incident angle θ_i, are also defined.

Further increasing n_a leads to a redshift of the resonance wavelength. We then calculate the colors supported by the reflection spectra as shown in the upper part of Fig. 2(a). The calculated colors are also employed to colorize the corresponding spectra. This scheme is also applied to the colors of other reflection spectra. It is obvious that the resulting colors maintain a whitish color, which are thus incapable of discriminating such a big index change via colors. A similar scenario takes place when P_x increases to 380 nm as shown in the upper part of Fig. 2(b).

However, the reflection line shape will be changed distinctly when an analyzer is inserted with an orientation angle φ_2, i.e., another linear polarizer, to select the polarization state of the specular reflection [25,26]. In particular, when the analyzer is oriented orthogonally ($\varphi_2 = 135°$) to the incident polarization, the line shape of the reflection spectra transforms from dips into peaks with a negligible background [25,26]. Meanwhile, the narrow full width at half-maximum (FWHM) is reserved with a considerable reflectivity at the resonance as shown in the lower part in Fig. 2(a). The resonance remains at 419 nm when $n_a = 1$. The maintained FWHM and resonance wavelength verifies the same origin of the resonance mode [25,26]. Remarkably, the generated color mutates from whitish to purple, as labeled in lower part of Fig. 2(a). Here, the reflected spectrum can be given as [25,26]

$$\frac{1}{\sqrt{2}} E_0 \left[a + \frac{b\Gamma_{\text{rab}} e^{i\delta}}{(\omega - \omega_0) + i\Gamma_{\text{tot}}} \right], \quad (3)$$

where E_0 is the incident field and ω_0 represents the resonance frequency; a and b are the amplitude of direct reflection and

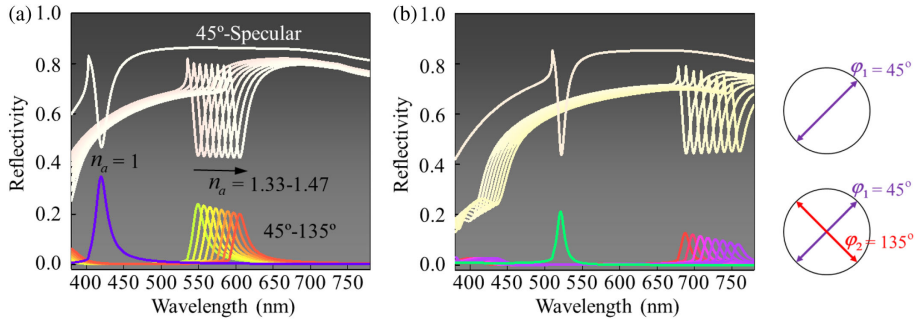

Fig. 2. Dependence of specular reflectivity on the reflective index of the immediate environment for (a) $P_x = 300$ nm and (b) $P_x = 380$ nm. Right column shows the polarizer-analyzer configuration used in calculation. In the right column, the purple arrow represents the polarization state of the incident light, and the red arrow indicates that only part specular reflection polarized along $\varphi_2 = 135°$ is collected. The colors of each reflection spectra are calculated using their corresponding spectra. Here $H = 100$ nm, $W = 150$ nm, and $L = P_x/2$. $P_y = 200$ nm for all the simulations. The incident angle is $\theta_i = 20°$ and the polarization angle of incident light is $\varphi_1 = 45°$.

SPP, respectively; δ denotes the phase difference between the SPP and reflection field; and Γ_{tot} is the total decay rate. The Jones matrix for the analyzer is $[1, -1; -1, 1]/2$ [30]. The corresponding reflection spectra can be expressed as $R_{45°-135°} = |b\Gamma_{\text{rab}}/4((\omega - \omega_0) + i\Gamma_{\text{tot}})|$, indicating that the reflection spectrum only contains a Lorentzian-type resonance without background. Hence, the dip of reflectance will convert to a peak through cross-polarization configuration. As a result, vivid colors can be observed under the 45°–135° configurations. Therefore, φ_2 is chosen to be 135° for colorimetric sensing [25,26]. As n_a increases to 1.33, the resonance peak shifts to 550 nm, and a yellow-green color is generated accordingly. As the index increases further, vibrant yellow-red colors are generated. Naturally, the index-dependent color changes can be potentially used for colorimetric sensing application.

When $P_x = 380$ nm, the resonance shifts to a longer wavelength, and some high-order SPP modes are involved. Nevertheless, the colors for the 45°-specular configuration remain whitish in different immediate environments, like the presented colors of the spectra shown in the upper part of Fig. 2(b). In sharp contrast, green-red-purple colors are observed for the 45°–135° configuration as shown in the lower part of Fig. 2(b). Although the magnitude of reflectivity decreases due to the lower excitation efficiency of SPP modes, the brightness of the expected color for visualization is still acceptable in contrast to a dark background as long as the power of the incident light is large enough. It is notable that higher-order SPP modes will be excited at ~ 400 nm for a larger refraction index, which contributes to the final colors via a mixture between the purple and the red.

As described in Eq. (1), the periodicity of the grating structures greatly affects the resonance spectrum position. Therefore, varying periodicity will alter the reflection spectrum or introduce new SPP modes in the visible range, which will result in a variation of the presented colors. We thus investigate the influence of P_x on the generated colors by calculating specular reflection under the 45°–135° configuration. The color is calculated as n_a increases from 1.33 to 1.47, corresponding to the index range of the general aqueous solution environment. The colors are plotted in Fig. 3 for P_x ranging from 260 to 400 nm. The colors shown in the first column on the left are calculated

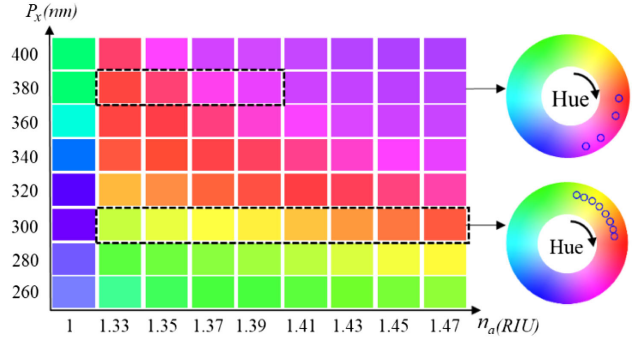

Fig. 3. Refractive index-dependent colors calculated for P_x increasing from 260 to 400 nm when $\theta_i = 20°$. The right insets are the progression of hue in a cylindrical cross section of the perceptually uniform LCh_{ab} color space for (bottom) $P_x = 300$ nm and (top) $P_x = 380$ nm, respectively. The open circles are associated colors encompassed by the black-dashed rectangular in the color map on the left.

when $n_a = 1$. As P_x increases, the color evolves from purple to green due to the redshift of resonance wavelength. When $P_x = 260$ nm, green is presented when a solvent is attached. In contrast, yellow and red gradually come out as P_x increases.

When $P_x = 380$ nm, the color variation can be discerned when the refractive index ranges from 1.33 to 1.39, as shown by the colors in the second row encompassed by the black-dashed box in Fig. 3. It is observed that the overall excited efficiency of the $(-1, 0)$ mode gradually decreases with the increased n_a, and the contribution from the $(1, 0)$ mode is elevated in color rendering. As the index increases from 1.41 to 1.47, the $(-1, 0)$ mode shifts to a longer wavelength. The presented colors remain indistinguishable purples as shown in the second row in Fig. 3. Such a scenario starts even at a smaller index $n_a = 1.35$ when $P_x = 400$ nm.

To quantitatively characterize the sensing performance of the proposed structure, the color parameters are converted from the Commission Internationale de l'Eclairage (CIE) map to LCh_{ab} space numerically [26]. The LCh_{ab} intuitively reflects the eye response to color changes that are uniform for any point in the cylindrical coordinates. Here the hue value is plotted along the angular direction in LCh_{ab} space. In particular, the colors for

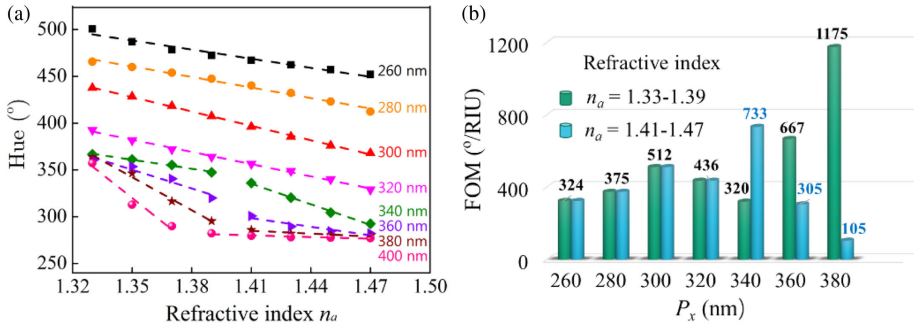

Fig. 4. (a) Dependence of hue of the presented color on the refractive index. (b) Dependence of FOM on the periodicity at two refractive index ranges. Here $\theta_i = 20°$.

$P_x = 300$ and 380 nm are presented in the right insets of Fig. 3, where open circles and black arrow indicate the corresponding colors in the LCh_{ab} map and the direction of increasing index, respectively.

Accordingly, a FOM is defined as $|\Delta H/\Delta n_a|$ to characterize the colorimetric sensing performance, where ΔH and Δn_a are the variation of hue value and the refractive index, respectively. As shown in Fig. 4(a), the dependence of hue on the refractive index is plotted for P_x ranging from 260 to 400 nm. For small periodicities, the hue value decreases linearly as n_a increases from 1.33 to 1.47, which indicates that the color evolves from green to red gradually as shown in the bottom right inset in Fig. 3. The linearity can be attributed to the sole excitation of the $(-1, 0)$ mode in the entire visible band, which is consistent with the reflection spectrum in Fig. 2(a). However, when $P_x > 340$ nm, it is obvious that the linear dependence of hue variation on n_a is broken due to the appearance of the other SPP modes. Above all, when $P_x > 360$ nm, a two-stage decrease trend is observed. The corresponding FOM is extracted as shown in the histogram in Fig. 4(b). When $P_x \leq 320$ nm, both the green and blue histogram pillars share the same FOM. When $P_x > 320$ nm, the green pillars represent the FOM for a small index range, and the blue ones represent the FOM for large index range. The FOM is stable for $P_x < 320$ nm and reaches 512°/RIU at $P_x = 300$ nm, which surpasses the FOM of 212.7°/RIU supported by localized surface plasmon resonances (LSPRs) [10]. In contrast, the FOM for large periodicity grows rapidly for the refractive index ranging from 1.33 to 1.39, which corresponds to common solutions such as water [31], ethanol [32], or other aqueous solutions [33]. When $P_x = 380$ nm, the FOM reaches 1175°/RIU. Moreover, when the P_x continues to increase to 400 nm, the introduced multiple modes, including $(-2, 0)$, $(1, 0)$, and $(-1, 0)$, lead to more complex color changes, which induces the largest FOM—as high as 1684°/RIU for an index restricted from 1.33 to 1.37. For $n_a > 1.37$, the $(-1, 0)$ mode gradually extends into the infrared range, and thus the colors remain almost the same. Therefore, in a more common aqueous environment with the index ranging from 1.33 to 1.37, the proposed plasmonic colorimetric sensing substrate shows a superior performance in the reddish region.

The properties of SPP modes are also affected by the incident angle. The reflection spectra at different incident angles are shown in Figs. 5(a) and 5(c) when $n_a = 1.33$. We thus calculate the dependence of FOM on the incident angle as shown in

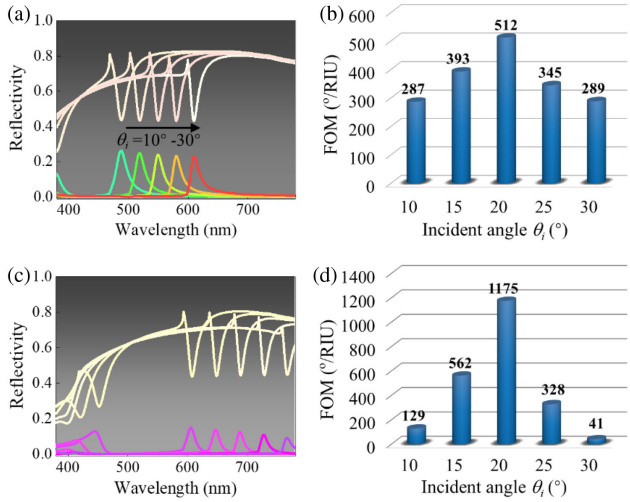

Fig. 5. Dependence of specular reflectivity on the incident angle for (a) $P_x = 300$ nm and (c) $P_x = 380$ nm, $n_a = 1.33$. Dependence of FOM on the incident angle for (b) $P_x = 300$ nm, $n_a = 1.33 - 1.47$ and (d) $P_x = 380$ nm, $n_a = 1.33 - 1.39$.

Fig. 5. As the incident angle varies from 10° to 30° at intervals of 5°, the FOM initially increases and reaches the maximum at 20°, and then it decreases. For small angles, multiple SPP modes coexist and contribute to the finally presented colors. As incident angle increases, for example, the $(1, 0)$ mode blueshifts, while the $(-1, 0)$ mode redshifts. Consequently, the reflection spectrum is gradually dominated by the $(-1, 0)$ mode since other modes shift out of the visible range as shown in Fig. 5(a). The color evolves from blue to green, yellow and red regions. The FOM thus increases as the angles increases and reaches its maximum of 512°/RIU when $\theta_i = 20°$. As the incident angle increases further, the presented colors gently locate in the range of yellow-reddish-purple, which has less variation in the LCh_{ab} color space. When the angle $\theta_i = 20°$, anticipated color changes are less pronounced than the case at $\theta_i = 20°$ for human eyes. Corresponding redshifted colors thus lead to a smaller FOM.

As P_x increases to 380 nm, a sharp change can be obtained by varying the incident angle. The appearance of the $(1, 0)$ SPP mode at the short wavelength range has great impact on the color rendering. Other angle-dependent high-order modes will also participate in color generation. Meanwhile, the wavelength spacing between the $(-1, 0)$ and other SPP modes at $\theta_i = 20°$

is larger than the counterparts at another incident angles, which produces a higher FOM, as shown in Figs. 5(c) and 5(d). As the incident angle further inclines, the resonance peaks of the (1, 0) and (−1, 0) modes keep shifting to shorter and longer wavelengths, and even shift beyond the range of visible light. Hence, an appropriate angle θ_i of the larger FOM ranging from 1.33 to 1.39 should be set at 20°. In addition, reasonable deviation of the both incident angle and the polarizer angles has little influence on the sensing performance of the system.

3. CONCLUSION

To conclude, we proposed a reflection-type colorimetric sensing substrate using plasmonic Al nanohole arrays. By inserting a polarizer-analyzer pair, vibrant colors can be generated covering from blue, to green, to red under the 45°–135° configuration. Significantly, the obvious color changes can be flexibly realized by controlling the period P_x and incident angle θ_i. It is found that the colorimetric FOM can reach 512°/RIU for a refractive index ranging from 1.33 to 1.47, while an even higher FOM can reach 1175°/RIU for a special index range, five-fold higher than previous works, in the demodulation of the hue [10]. In addition, it can readily satisfy the requirements for miniaturization and integration with other instruments. Furthermore, the proposed colorimetric sensing substrate can be fabricated using focused ion beam (FIB) [34] or electron beam lithography (EBL) [10,19,35]. We thus believe that the proposed colorimetric sensing substrate holds great promise to be applied in rapid identification of analytes in aqueous solutions.

Funding. National Natural Science Foundation of China (11604256); Natural Science Foundation of Shaanxi Province (2018JM6001); Fundamental Research Funds for the Central Universities of Xi'an Jiaotong University (Z201805196); Fundamental Research Funds for the Central Universities of Shaanxi Normal University (GK201803016).

REFERENCES

1. J. Homola, S. S. Yee, and G. Gauglitz, "Surface plasmon resonance sensors: review," Sensor Actuat. B Chem. **54**, 3–15 (1999).
2. J. Homola, "Surface plasmon resonance sensors for detection of chemical and biological species," Chem. Rev. **108**, 462–493 (2008).
3. X. Guo, "Surface plasmon resonance based biosensor technique: a review," J. Biophoton. **5**, 483–501 (2012).
4. Z. L. Cao, S. L. Wong, S. Y. Wu, H. P. Ho, and H. C. Ong, "High performing phase-based surface plasmon resonance sensing from metallic nanohole arrays," Appl. Phys. Lett. **104**, 171116 (2014).
5. M. H. Elshorbagy, A. Cuadrado, and J. Alda, "High-sensitivity integrated devices based on surface plasmon resonance for sensing applications," Photon. Res. **5**, 654–661 (2017).
6. Y. Cheng, X. S. Mao, C. Wu, and L. Wu, "Infrared non-planar plasmonic perfect absorber for enhanced sensitive refractive index sensing," Opt. Mater. **53**, 195–200 (2016).
7. Y. Cheng, H. Zhang, X. S. Mao, and R. Z. Gong, "Dual-band plasmonic perfect absorber based on all-metal nanostructure for refractive index sensing application," Mater. Lett. **219**, 123–126 (2018).
8. H. Zou and Y. Cheng, "Design of a six-band terahertz metamaterial absorber for temperature sensing application," Opt. Mater. **88**, 674–679 (2019).
9. Y. Cheng, H. Luo, F. Chen, and R. Gong, "Triple narrow-band plasmonic perfect absorber for refractive index sensing applications of optical frequency," OSA Continuum **2**, 2113–2122 (2019).
10. N. S. King, L. Liu, X. Yang, B. Cerjan, H. O. Everitt, P. Nordlander, and N. J. Halas, "Fano resonant aluminum nanoclusters for plasmonic colorimetric sensing," ACS Nano **9**, 10628–10636 (2015).
11. M. J. Crow, K. Seekell, and A. Wax, "Polarization mapping of nanoparticle plasmonic coupling," Opt. Lett. **36**, 757–759 (2011).
12. M. Serhatlioglu, S. Ayas, N. Biyikli, A. Dana, and M. E. Solmaz, "Perfectly absorbing ultra thin interference coatings for hydrogen sensing," Opt. Lett. **41**, 1724–1727 (2016).
13. S. Ayas, G. Bakan, E. Ozgur, K. Celebi, G. Torunoglu, and A. Dana, "Colorimetric detection of ultrathin dielectrics on strong interference coatings," Opt. Lett. **43**, 1379–1382 (2018).
14. K. V. Sreekanth, Y. Alapan, M. Elkabbash, E. Ilker, M. Hinczewski, U. A. Gurkan, A. D. Luca, and G. Strangi, "Extreme sensitivity biosensing platform based on hyperbolic metamaterials," Nat. Mater. **15**, 621 (2016).
15. A. A. Yanik, A. E. Cetin, M. Huang, A. Artar, S. H. Mousavi, A. Khanikaev, J. H. Connor, G. Shvets, and H. Altug, "Seeing protein monolayers with naked eye through plasmonic Fano resonances," Proc. Natl. Acad. Sci. USA **108**, 11784–11789 (2011).
16. Y. Yang, I. I. Kravchenko, D. P. Briggs, and J. Valentine, "All-dielectric metasurface analogue of electromagnetically induced transparency," Nat. Commun. **5**, 5753 (2014).
17. Y. Deng, G. Cao, H. Yang, G. Li, X. Chen, and W. Lu, "Tunable and high-sensitivity sensing based on Fano resonance with coupled plasmonic cavities," Sci. Rep. **7**, 10639 (2017).
18. H. J. Hu, F. W. Zhang, G. Zhang, J. Y. Chen, Q. Li, and L. J. Wu, "Fano resonances with a high figure of merit in silver oligomer systems," Photon. Res. **6**, 204–213 (2018).
19. X. Xu, B. Peng, D. Li, J. Zhang, L. M. Wong, Q. Zhang, S. Wang, and Q. Xiong, "Flexible visible-infrared metamaterials and their applications in highly sensitive chemical and biological sensing," Nano Lett. **11**, 3232–3238 (2011).
20. X. Wang, T. W. Chang, G. Lin, M. R. Gartia, and G. L. Liu, "Self-referenced smartphone-based nanoplasmonic imaging platform for colorimetric biochemical sensing," Anal. Chem. **89**, 611–615 (2016).
21. X. Li, X. Gao, W. Shi, and H. Ma, "Design strategies for water-soluble small molecular chromogenic and fluorogenic probes," Chem. Rev. **114**, 590–659 (2014).
22. T. Minamia, F. Emamia, R. Nishiyabuc, Y. Kuboc, and P. Anzenbacher, Jr., "Quantitative analysis of modeled ATP hydrolysis in water by a colorimetric sensor array," Chem. Commun. **52**, 7838–7841 (2016).
23. S. J. Tan, L. Zhang, D. Zhu, X. M. Goh, Y. M. Wang, K. Kumar, C. W. Qiu, and J. K. W. Yang, "Plasmonic color palettes for photorealistic printing with aluminum nanostructure," Nano Lett. **14**, 4023–4029 (2014).
24. M. König, M. Rahmani, L. Zhang, D. Y. Lei, T. R. Roschuk, V. Giannini, C.-W. Qiu, M. Hong, S. Schlücker, and S. A. Maier, "Unveiling the correlation between nanometer-thick molecular monolayer sensitivity and near-field enhancement and localization in coupled plasmonic oligomers," ACS Nano **8**, 9188–9198 (2014).
25. L. Zhang, C. Y. Chan, J. Li, and H. C. Ong, "Rational design of high performance surface plasmon resonance sensors based on two-dimensional metallic hole arrays," Opt. Express **20**, 12610–12621 (2012).
26. L. Cheng, K. Wang, J. Mao, X. M. Goh, Z. Chu, Y. Zhang, and L. Zhang, "Extrinsic polarization-enabled covert plasmonic colors using aluminum nanostructures," Ann. Phys. (Berlin) **531**, 1900073 (2019).
27. E. D. Palik, *Handbook of Optical Constants of Solids* (Academic, 1985), Vol. **1**.
28. D. Y. Lei, J. Li, A. I. Fernández-Domínguez, H. C. Ong, and S. A. Maier, "Geometry dependence of surface plasmon polariton lifetimes in nanohole arrays," ACS Nano **4**, 432–438 (2010).
29. Z. L. Cao and H. C. Ong, "Study of the momentum-resolved plasmonic field energy of Bloch-like surface plasmon polaritons from periodic nanohole array," Opt. Express **25**, 296640 (2017).
30. E. Hecht, *Optics*, 4th ed. (Addison Wesley, 2001).
31. N. Liu, T. Weiss, M. Mesch, L. Langguth, U. Eigenthaler, M. Hirschere, C. Sonnichsen, and H. Giessen, "Planar metamaterial analogue of

electromagnetically induced transparency for plasmonic sensing," Nano Lett. **10**, 1103–1107 (2010).
32. A. V. Kabashin, P. Evans, S. Pastkovsky, W. Hendren, G. A. Wurtz, R. Atkinson, R. Pollard, V. A. Podolskiy, and A. V. Zayats, "Plasmonic nanorod metamaterials for biosensing," Nat. Mater. **8**, 867–871 (2009).
33. https://www.engineeringtoolbox.com/refractive-index-d_1264.html.
34. S. Yokogawa, S. P. Burgos, and H. A. Atwater, "Plasmonic color filters for CMOS image sensor applications," Nano Lett. **12**, 4349–4354 (2012).
35. V. R. Shrestha, S. S. Lee, E. S. Kim, and D. Y. Choi, "Polarization-tuned dynamic color filters incorporating a dielectric-loaded aluminum nanowire array," Sci. Rep. **5**, 12450 (2015).